

# Experimental and Numerical Investigation on the Triaxial Compressive Behavior of Steamed Recycled Aggregate Concrete

Yuzhi Chen <sup>1,2</sup>, Yingjie Ning <sup>3</sup>, Xudong Chen <sup>2</sup>, Weihong Xuan <sup>1,\*</sup> and Xiangyi Zhu <sup>4</sup>

<sup>1</sup> School of Architectural Engineering, Jinling Institute of Technology, Nanjing 211169, China

<sup>2</sup> College of Civil and Transportation Engineering, Hohai University, Nanjing 210098, China

<sup>3</sup> Zhejiang Communications Construction Group Co., Ltd., Hangzhou 310051, China

<sup>4</sup> College of Water Conservancy & Hydropower Engineering, Hohai University, Nanjing 210098, China

\* Correspondence: xwh@jit.edu.cn

**Abstract:** The use of recycled aggregates to produce precast concrete products is conducive to the green development of construction industrialization. This paper aimed to study the effects of curing regimes and confining pressures on the triaxial compression behavior of recycled aggregate concrete (RAC). Triaxial compression tests were carried out on RAC under different curing regimes (standard curing, 60 °C—12 h and 80 °C—9 h), and the designed confining pressures were 0 MPa, 2.5 MPa, 5 MPa, and 10 MPa. The results show that the increase of confining pressure limits the expansion of cracks, causing the failure mode to change from vertical splitting to oblique shearing, and the triaxial compressive strength is doubled at most. Compared with standard curing, steam curing significantly weakened the triaxial compressive strength of RAC, which was related to the reduction of RAC cohesion, and the cohesion of RAC steam cured at 80 °C was reduced by 30%. The triaxial compression failure of RAC closely follows the Mohr–Coulomb criterion. Based on the discrete element method and test results, an RAC triaxial compression numerical model considering the shape of the actual coarse aggregate was established, and the propagation of cracks was discussed at the mesoscopic level.

**Keywords:** recycled aggregate concrete (RAC); steam curing; triaxial compressive; mesoscopic simulation

**Citation:** Chen, Y.; Ning, Y.; Chen, X.; Xuan, W.; Zhu, X. Experimental and Numerical Investigation on the Triaxial Compressive Behavior of Steamed Recycled Aggregate Concrete. *Buildings* **2023**, *13*, 334. <https://doi.org/10.3390/buildings13020334>

Academic Editor: Jorge de Brito

Received: 22 December 2022

Revised: 14 January 2023

Accepted: 19 January 2023

Published: 23 January 2023



**Copyright:** © 2023 by the authors. Licensee MDPI, Basel, Switzerland. This article is an open access article distributed under the terms and conditions of the Creative Commons Attribution (CC BY) license (<https://creativecommons.org/licenses/by/4.0/>).

## 1. Introduction

As the most widely used building material, concrete has played a huge role in the evolution of modern society. However, the massive use of concrete inevitably brings some problems. On the one hand, the huge consumption of sand and gravel resources, as well as cement production accompanied by a large number of CO<sub>2</sub> emissions, results in serious environmental disruption [1,2]. On the other hand, the accumulation of waste concrete occupies massive land resources and causes environmental pollution. Processing waste concrete into recycled aggregate (RA) for the manufacture of recycled aggregate concrete (RAC) can not only reduce the environmental pressure, but also greatly reduce the exploitation of natural resources [3–5].

Many scholars have carried out plenty of experimental and theoretical research on RAC, which greatly enriches the research findings of RAC [6–9]. However, current research on RAC is mainly focused on the mix design [10,11], the modification of RA [12,13], and the strength and durability of RAC [14,15]. The research on the mechanical properties of RAC is mostly carried out under uniaxial stress. Nevertheless, the concrete of engineering structures is often subject to complex multiaxial stress [16], such as concrete-filled steel tubes, concrete confined by stirrups, and tunnel segments. The multiaxial strength and

deformation characteristics of concrete are very different from those under uniaxial stress [17]. The findings suggest that the confinement of steel tubes can improve the strength and ductility of RAC, but the influence of the RA content is relatively low [18,19]. Lateral constraints also significantly affect the failure mode of RAC, which will transfer from vertical split failure to oblique shear failure with the increase of confining pressure [20]. It is necessary to study the mechanical behaviors and damage mechanism of RAC under triaxial stress for promoting the engineering application of RAC.

Furthermore, in the context of the industrialization of construction, prefabrication has become the main construction method for concrete elements [21,22]. Steam curing is conducive to rapidly increasing the early strength of precast concrete elements, thereby reducing demolding time and raising production efficiency [23]. However, studies show that excessive curing temperature or time may adversely affect the mechanical properties of concrete [24,25]. Compared with ordinary concrete, research on the effect of steam curing on the mechanical properties of RAC is insufficient, resulting in the lack of adequate experimental data and theory for the design safety and rationality of prefabricated RAC components.

To explore the strength and failure process of RAC under triaxial stress, as well as the effect of steam curing, triaxial compression tests were carried out on RAC with different curing conditions (standard curing, 60 °C—12 h, and 80 °C—9 h) and different confining pressures (0 MPa, 2.5 MPa, 5 MPa, and 10 MPa). Based on the Mohr–Coulomb criterion, a triaxial compression failure model reflecting the influence of curing conditions was established to study the effect of steam curing on cohesion and the internal friction angle of RAC. A numerical model considering the morphology and distribution of recycled aggregates was established, the damage effect caused by steam curing was integrated into the mesoscopic parameters, and the triaxial mechanical behavior and damage mechanism of RAC under different curing conditions and confining pressures were analyzed.

## 2. Experiments

### 2.1. Materials

Recycled aggregates with a maximum particle size of 26.5 mm, bulk density of 1264.5 kg/m<sup>3</sup>, and crushing value of 15.2% are used as coarse aggregates. River sand, with a fineness modulus of 2.5, is used as fine aggregate. The grading curves of recycled aggregates and river sand are shown in Figure 1. P·O 42.5 ordinary Portland cement with a specific surface of 320 m<sup>2</sup>/kg, an initial setting time of 55 min, and a final setting time of 310 min, and ground granulated blast furnace slag are used as binding materials. The relevant chemical composition contents are shown in Table 1. The mix proportion of RAC is shown in Table 2 and the fresh mixture has a good fluidity with the measured slump between 190 mm and 200 mm. The mixture was mixed for two minutes before being molded, and then vibrated for 15 s. The mixture was demolded after one day and cured according to different curing regimes.

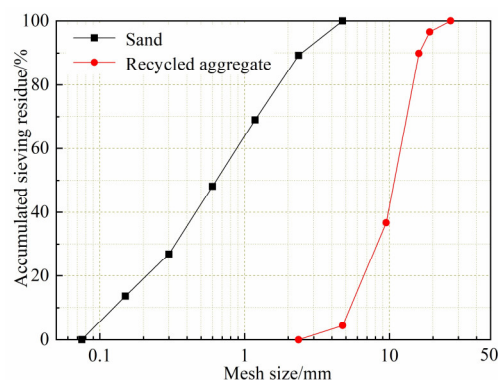


Figure 1. Grading curves of the aggregate.

**Table 1.** Chemical component content of cementitious material (%).

Components	CaO	MgO	SiO <sub>2</sub>	Fe <sub>2</sub> O <sub>3</sub>	P <sub>2</sub> O <sub>5</sub>	Al <sub>2</sub> O <sub>3</sub>	SO <sub>3</sub>	LOI
Slag	45.09	6.99	27.33	0.45	0.13	13.66	4.03	0.95
Cement	54.65	2.58	22.07	4.32	1.03	6.30	2.59	2.14

**Table 2.** Mix proportion of RAC (kg/m<sup>3</sup>).

Cement	Slag	Sand	RA	Water	Water Reducer
241.5	241.5	815	957	145	3.42

## 2.2. Curing Regimes

### (1) Standard curing

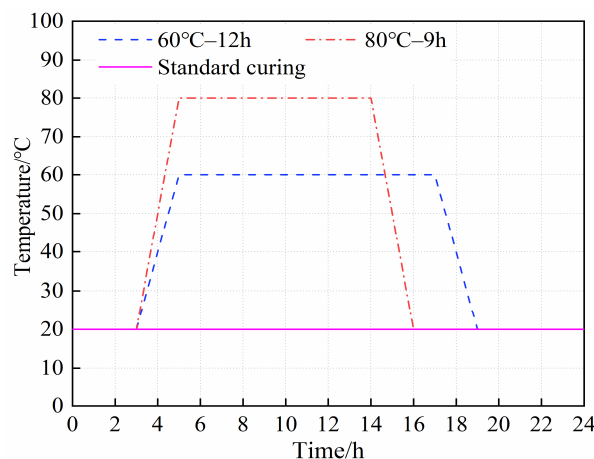
The specimens were covered with films after casting and demolded after one day. The compression tests were carried out after curing for 90 days in a standard curing room with a temperature of  $20 \pm 2$  °C and a humidity of 95%.

### (2) Steam curing

The steam curing process can be divided into the static stop stage, the heating stage, the constant temperature stage, and the cooling stage. Steam curing can improve the early strength of concrete, but excessive temperature and time will reduce the late strength and consume more energy [26]. In this study, two steam curing regimes of 60 °C–12 h and 80 °C–9 h were adopted. The detailed curing temperature and time are shown in Table 3. The static stop stage started from the pouring of RAC into the mold and it was kept at 20 °C for 3 h. The heating stage lasted for 2 h, from 20 °C to the target temperature (60 °C and 80 °C). At the constant temperature stage, the curing time was 12 h and 9 h, respectively, at the target steam curing temperature. The cooling stage lasted for 2 h, from the target steam curing temperature to 20 °C. The curves of the curing temperature versus time are shown in Figure 2. After steam curing, the specimens were demolded and placed into the standard curing room for 90 days. After that, cylinder specimens with a diameter of 50 mm and a height of 100 mm were made by coring and cutting for the triaxial compression test.

**Table 3.** Control parameters of the steam curing system.

Static Stop Time/h	Heating Time/h	Constant Temperature/°C	Holding Time/h	Cooling Time/h
3	2	60	12	2
		80	9	

**Figure 2.** The curves of curing temperature versus time.

For clarity, the specimens under standard curing, 60 °C steam curing for 12 h, and 80 °C steam curing for 9 h are marked as RAC20, RAC6012, and RAC8009, respectively.

### 2.3. Triaxial Compression Test

The triaxial compression test of RAC was conducted in the TOP INDUSTRIE test system, as shown in Figure 3. The two loading methods of displacement control and stress control can be switched automatically. In the triaxial loading process, the confining pressure was firstly applied to specimen at a speed of 4.0 MPa/min and kept constant after reaching the target value. Then, the displacement control method was switched to apply the axial pressure with a loading rate of 0.5  $\mu\text{m/s}$ . Two LVDTs were used to measure the axial deformation. Triaxial compression tests under four confining pressures ( $\sigma_3$ ) of 0 MPa, 2.5 MPa, 5 MPa, and 10 MPa were carried out. Under each curing regime and confining pressure, three specimens were prepared for repeated testing, with a total of 36 samples.

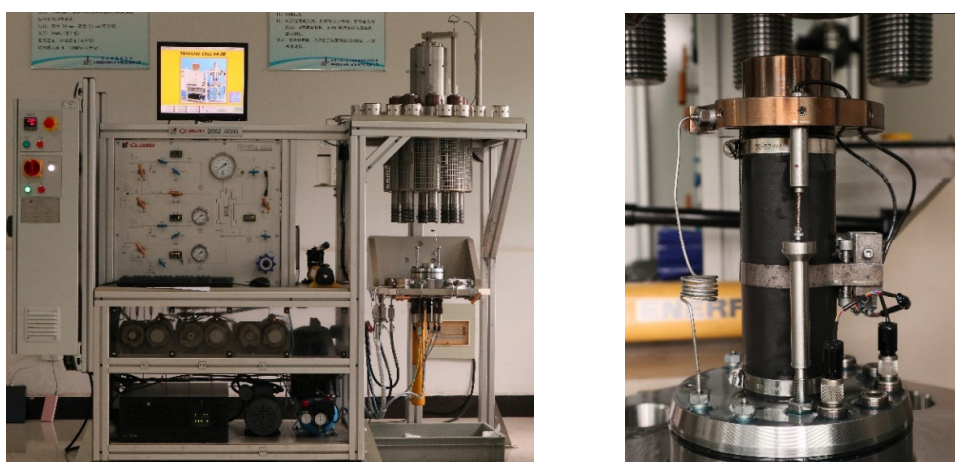
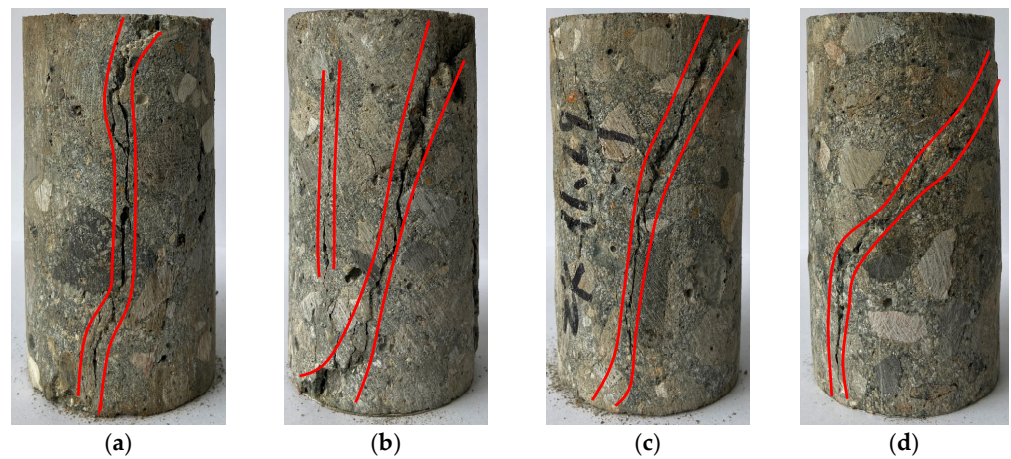


Figure 3. Triaxial compression test equipment.

## 3. Test Results and Analysis

### 3.1. Failure Mode

Figures 4 and 5 illustrate the influence of confining pressures and curing conditions on the failure mode of RAC, respectively. It can be seen from Figure 4a that the specimen exhibits a longitudinal splitting failure mode and obvious brittleness when without confining pressure. As the confining pressure increases, the inclination of the failure surface increases. The lateral constraint of the confining pressure inhibits the development of cracks, and the maximum volume strain increases with the increase of confining pressure, which makes the development path of the cracks change from vertical splitting to oblique shearing. Figure 5 illustrates that, under the confining pressure of 2.5 MPa, all three specimens exhibited shear failure characteristics, among which the oblique shear failure of RAC20 and RAC6012 is more obvious. The main failure plane of RAC8009 with the lowest strength has a smaller inclination angle, which is close to a vertical splitting failure and is accompanied by several small vertical cracks.



**Figure 4.** Failure modes of RAC8009 under different confining pressures. (a)  $\sigma_3=0$  MPa, (b)  $\sigma_3=2.5$  MPa, (c)  $\sigma_3=5$  MPa, (d)  $\sigma_3=5$  MPa.

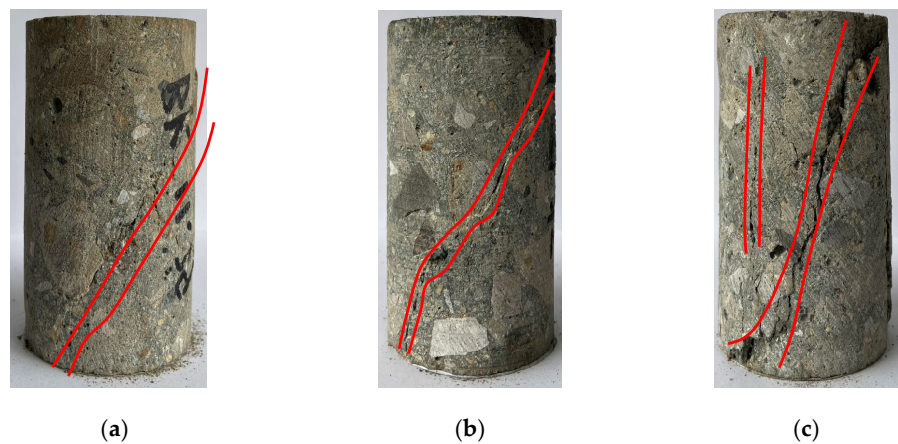


**Figure 5.** Failure modes of RAC under a confining pressure of 2.5 MPa. (a) RAC20, (b) RAC6012, (c) RAC8009.

### 3.2. Stress–Strain Curves

Figure 6 illustrates the stress–strain curves of different specimens. It can be seen that the peak deviatoric stress ( $\sigma_1-\sigma_3$ ) and peak strain of RAC increase significantly with the increase of the confining pressure. The stress–strain curve after the peak falls more slowly, indicating that the confining pressure enhances the deformability of RAC. Figure 7 illustrates the variation trend of the peak stress of the specimens under different confining pressures. For RAC20, the peak deviatoric stress increases from 69.18 MPa to 115.97 MPa as the confining pressure increases from 0 MPa to 10 MPa, with an increase of 67.6%. For RAC6012 and RAC8009, the peak deviatoric stress increases by 74.7% and 102.2%, respectively, when the confining pressure increases from 0 MPa to 10 MPa. High-temperature steam curing reduces the compressive strength of RAC, but steam-cured concrete is more sensitive to the constraint effect, and the strength increases more under the same confining pressure. As the steam curing temperature increases, the proportion of large capillary pores in concrete increases, and the shape of the pores becomes more complex, resulting in a decrease of compressive strength [27–29]. The lower the strength, the more obvious the improvement of its strength and deformation caused by confining pressure [30,31].

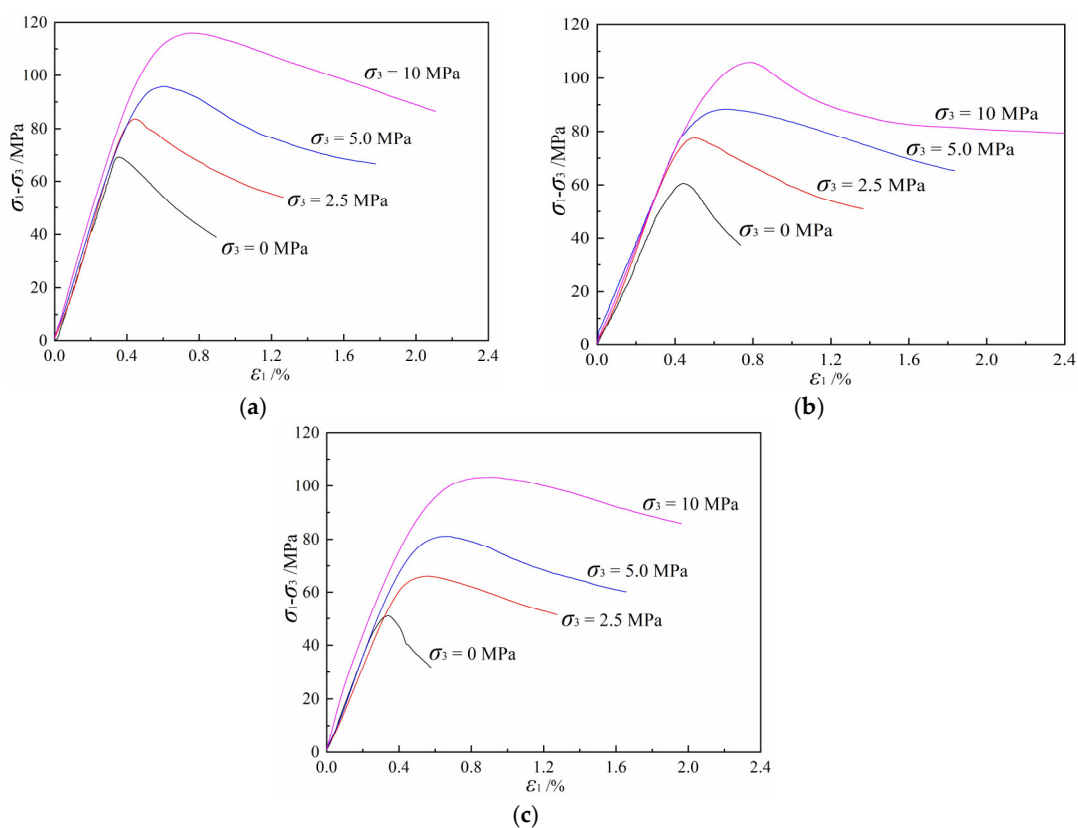


**Figure 6.** Triaxial stress–strain curves of RAC under different curing conditions. (a) RAC20, (b) RAC6012, (c) RAC8009.

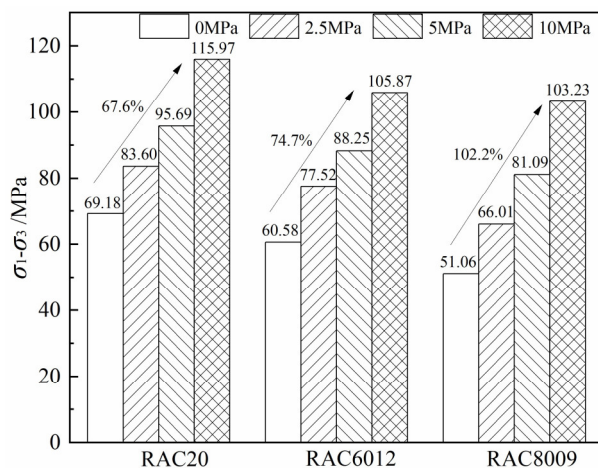


**Figure 7.** Effect of confining pressure on peak deviatoric stress.

### 3.3. The Cohesion and Internal Friction Angle

Previous studies have shown that the test results of concrete under triaxial compression are in good agreement with the Mohr–Coulomb criterion [32,33]. Based on the criterion shown in Figure 8, a triaxial failure model of RAC considering curing conditions can be established, as shown in Equation (1):

$$\frac{\sigma_1 - \sigma_3}{2} = \frac{\sigma_1 + \sigma_3}{2} \sin \varphi + c \cos \varphi \tag{1}$$

where  $\sigma_1$  is the maximum principal stress of RAC under different curing conditions;  $\sigma_3$  is the applied confining pressure;  $c$  and  $\varphi$  are the cohesion and internal friction angle of RAC

under different curing conditions. Equation (2) can be obtained by a simple transformation of Equation (1):

$$Y = X \sin \varphi + c \cos \varphi \quad (2)$$

where  $Y = \frac{\sigma_1 - \sigma_3}{2}$ ,  $X = \frac{\sigma_1 + \sigma_3}{2}$ .

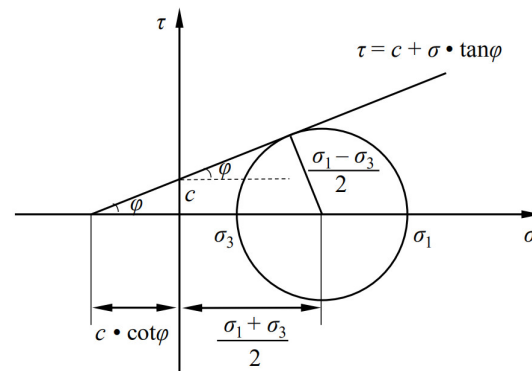


**Figure 8.** Schematic diagram of the Mohr–Coulomb criterion.

On the basis of the triaxial compression test results of RAC under different confining pressures and curing conditions, the values of  $c$  and  $\varphi$  are determined by linear regression. Figure 9 illustrates the fitting curves, and the related fitting parameters are shown in Table 4. The goodness of fit close to 1 indicates that  $c$  and  $\varphi$  of RAC under different curing conditions can be obtained exactly by the Mohr–Coulomb criterion.

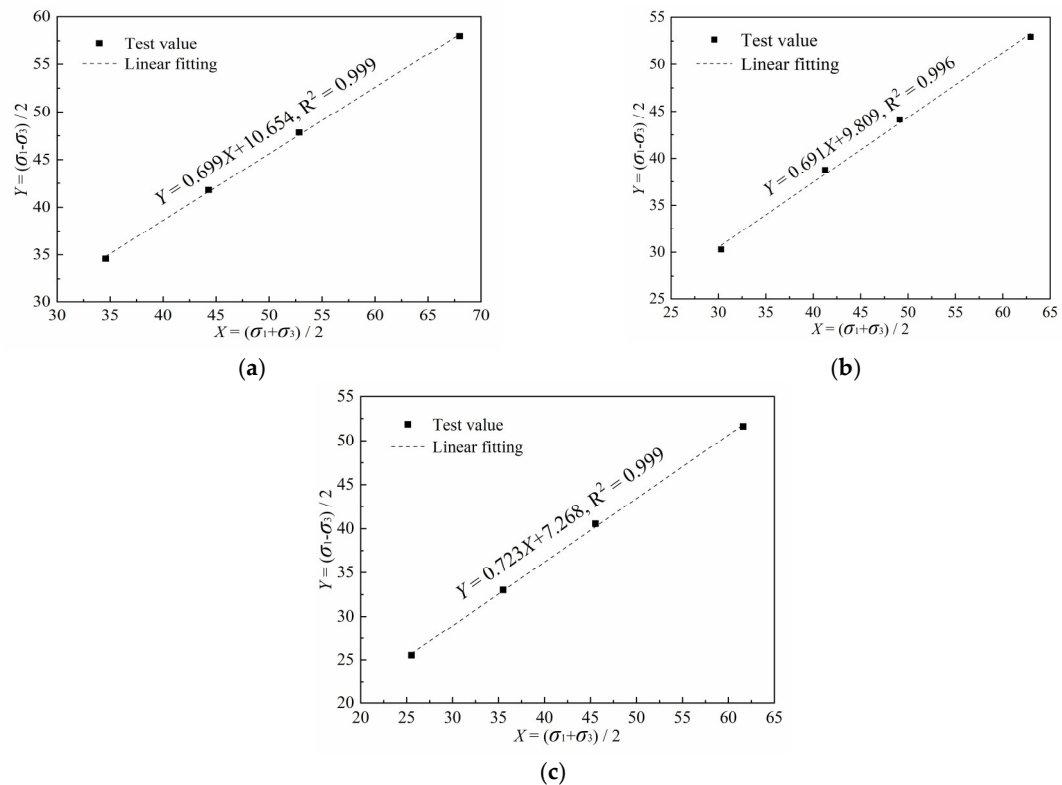


**Figure 9.** Calculation process of  $c$  and  $\varphi$  of RAC under different curing conditions. (a) RAC20, (b) RAC6012, (c) RAC8009.

**Table 4.** Fitting parameters determined by the Mohr–Coulomb criterion.

Fitting Parameters	Curing Conditions		
	RAC20	RAC6012	RAC8009
Slope ( $\sin\varphi$ )	0.699	0.691	0.723
Intercept ( $c\cos\varphi$ )	10.654	9.809	7.268
Degree of fit ( $R^2$ )	0.999	0.996	0.999

The values of  $c$  and  $\varphi$  are listed in Table 5. Compared with the standard-cured RAC, the  $c$  of RAC6012 and RAC8009 show 8.9% and 29.4% of reduction, respectively, while the  $\varphi$  of RAC8009 is the largest. The cohesion  $c$  of concrete materials depends on the composition of aggregate, cementitious material, and porosity. Higher steam curing temperatures increase the proportion of large capillary pores and the complexity of the pore shapes, causing an apparent reduction in cohesion. The increase of the internal friction angle  $\varphi$  seems to increase the confining pressure sensitivity of RAC.

**Table 5.**  $c$  and  $\varphi$  of RAC under different curing conditions.

Parameters	Curing Conditions		
	RAC20	RAC6012	RAC8009
Cohesion ( $c$ )/MPa	14.90	13.57	10.52
Internal friction angle ( $\varphi$ )/°	44.36	43.71	46.31

#### 4. Numerical Simulation

In this section, a numerical model with real coarse aggregate morphology was established and, based on the experimental results above, the influence of high-temperature steam curing on cohesion  $c$  and internal friction angle  $\varphi$  was integrated into meso-parameters. The experimental and simulation results were compared to further investigate the internal crack development and damage mechanism of steam-cured RAC under a triaxial load.

##### 4.1. Numerical Model

The discrete element method (DEM) was created by Cundall and Strack [34] to simulate the mechanical behavior of granular materials and was widely applied to rock, soil, concrete, and other materials. In this study, the numerical simulation was carried out based on the particle flow program PFC3D developed by DEM. In PFC3D, particles with a finite mass interact through internal forces and moments, and the motion of particles follows Newton's second law [35]. The contact constitutive of steam-cured RAC adopted the linear parallel bonding model, in which the bonding between two contacting particles is highly similar to the mechanical behavior of cement-based materials [36].

To simulate the triaxial compressive properties of steam-cured RAC more realistically, a numerical model based on the actual coarse aggregate morphology was established. In this study, the 3D geometry of the recycled aggregates generated by 3D scanning technology were created in PFC3D to simulate real coarse aggregates, whereas fine aggregates were simplified to rigid spheres. The RAC numerical model with a diameter of 50 mm and a height of 100 mm was generated, as shown in Figure 10a. Among them, coarse aggregates with a particle size of 5 mm to 26.5 mm account for 40% of the total aggregates, and the particle size of the fine aggregate is between 2 mm and 5 mm.

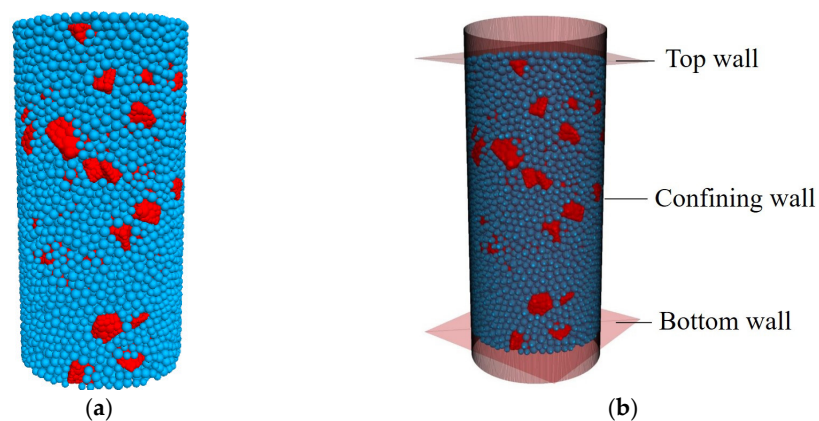


**Figure 10.** (a) Numerical model based on real aggregates; (b) Schematic diagram of loading.

The triaxial loading procedure of the RAC numerical model corresponding to the experiment was as follows: firstly, the confining wall was contracted until the confining pressure reached the target value; then, the top wall was moved down to apply axial pressure and the loading rate was set to  $0.5 \mu\text{m/s}$ . When applying axial pressure, servo control was used to dynamically adjust the confining wall to keep constant confining pressure. The triaxial loading model is shown in Figure 10b.

#### 4.2. Parameter Calibration

In this study, the parameter calibration was achieved by adjusting the mesoscopic parameters until the numerical simulation results were consistent with the experimental results. RAC with different curing conditions (standard curing,  $60^\circ\text{C}-12\text{ h}$ , and  $80^\circ\text{C}-9\text{ h}$ ) requires calibration of multiple sets of model parameters. In this study, the parameter calibration of standard-cured specimens was taken as the benchmark, and then the influence of the steam curing damage obtained by the experimental results was introduced into the benchmark, which simplified the calibration procedure.

The stress–strain curves of the numerical simulation and the experiment of standard-cured RAC are shown in Figure 11. It can be seen that there is a slight deviation between the simulated and experimental results. Compared with the smooth simulated curve, the experimental curve fluctuates slightly. This may be due to the existence of a certain number of pore defects in the sample. Under the triaxial load, the pore defects will be compacted, resulting in the fluctuation of the curve. The numerical model ignores the influence of these factors, and the curve behaves smoother.

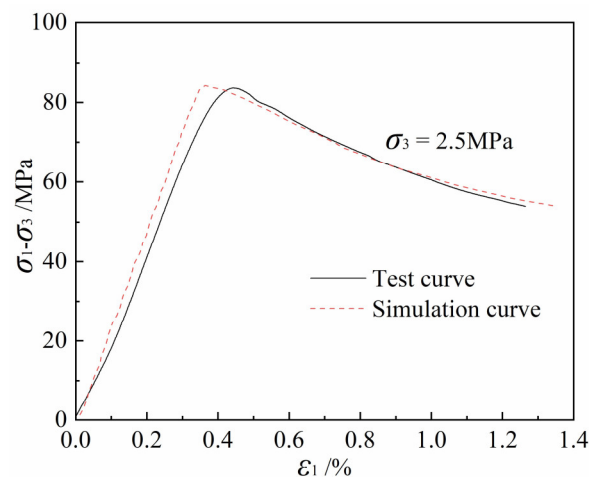


**Figure 11.** Comparison of simulated and experimental stress–strain curves (RAC20, confining pressure 2.5 MPa).

Figure 12 illustrates the experimental failure mode and the internal fracture development form of the numerical model. The failure modes obtained by simulation and experiment are close, and the penetrating oblique macroscopic cracks show obvious shear failure. In addition, the cracks are divided into shear and tensile failure in Figure 12b.

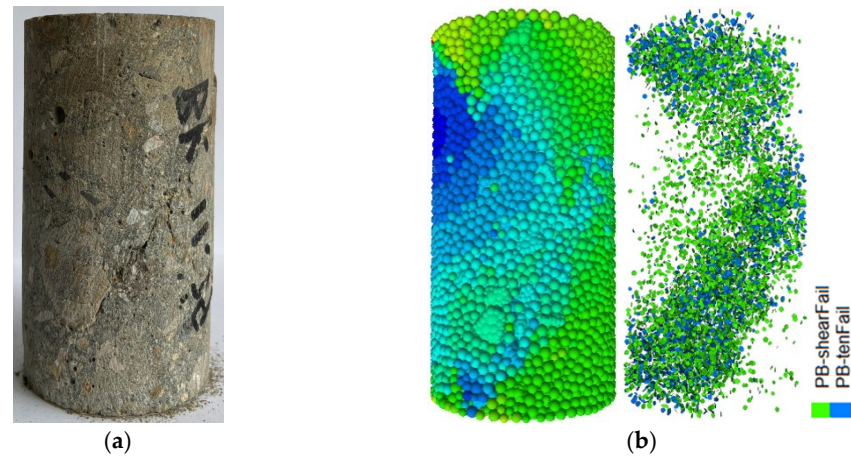
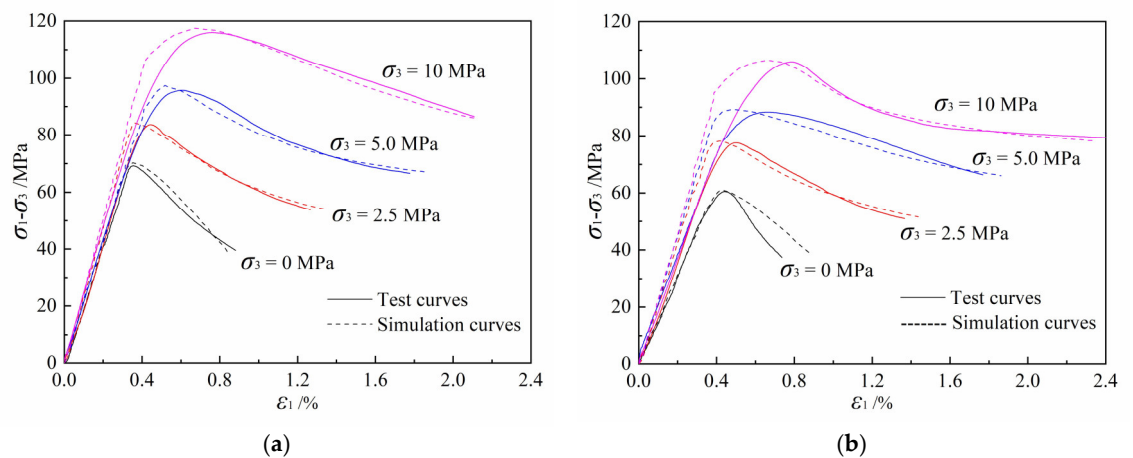


**Figure 12.** (a) Test failure mode; (b) Model failure mode and internal crack development (RAC20, confining pressure 2.5 MPa).

From the pattern of internal cracks, it can be seen that a small amount of tensile cracks generated on the top and bottom of the model at the initial stage of loading. Subsequently, a large number of shear cracks formed in the middle and lower part of the sample, and the propagation and penetration of shear cracks finally formed a macroscopic fracture surface.

#### 4.3. Numerical Results and Analysis

The numerical simulation of triaxial compression of RAC with different curing conditions and confining pressures was carried out. The comparison of the simulation results and the test curves is shown in Figure 13. The simulation results are in good agreement with the test stress–strain curves, indicating that the model can better reflect the triaxial mechanical properties of RAC under different confining pressures.



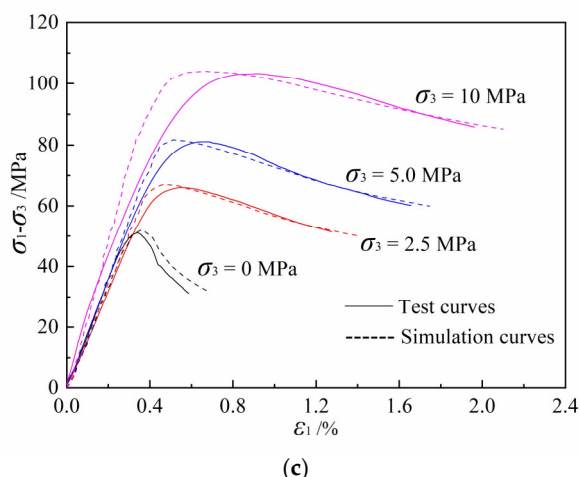


**Figure 13.** Comparison of simulation and test results of RAC under different curing conditions and confining pressures. (a) RAC20, (b) RAC6012, (c) RAC8009.

The formation and development of internal cracks in the specimen can be reproduced through numerical simulation. Taking the standard curing specimen RAC20 as an example, the failure and internal cracks of the specimen under different confining pressures are shown in Figure 14. Figures 15–17 show the crack growth process of RAC20, RAC6012, and RAC8009 under different confining pressures, respectively, including shear cracks, tensile cracks, and the total number of cracks. The cracks were extracted in PFC3D by Fish language, which helps us understand the damage mechanism of RAC from the mesoscopic level. It can be seen from Figure 15 that the lateral constraint limits the development of cracks to a certain extent. With the increase of confining pressure, the crack development process in the specimen is slower. Before the final failure of the specimen, under the same compressive deformation, the number of cracks decreases with the increase of confining pressure, but in the final failure, the number of cracks increases due to the more sufficient development of cracks in the specimen under the constraint of confining pressure, and the number of cracks is larger than that of uniaxial loading under 0 confining pressure. The 60 °C–12 h and 80 °C–9 h steam-cured specimens also show similar crack development trends, as shown in Figures 16 and 17, respectively.

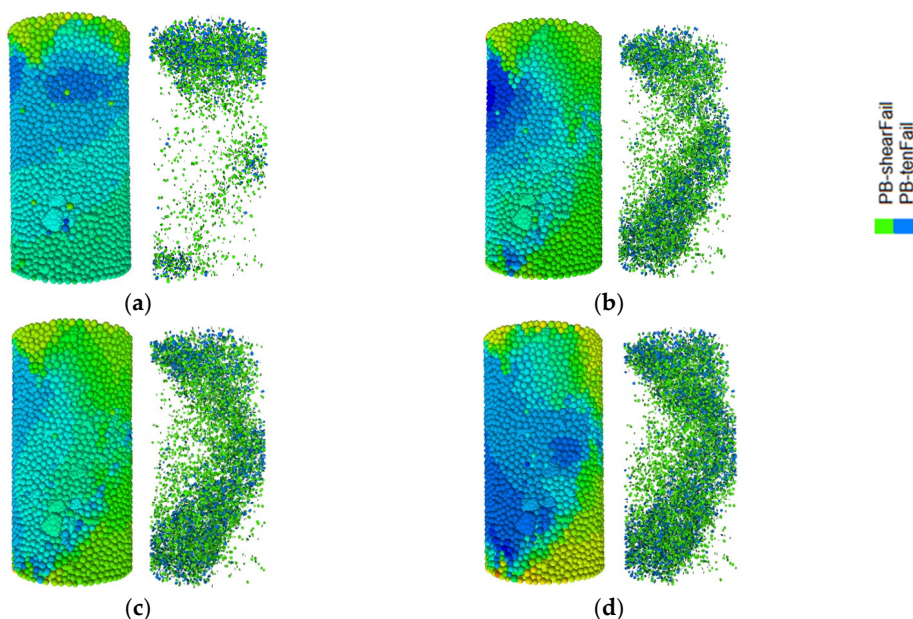


**Figure 14.** Damage simulation of RAC20 under different confining pressures. (a) 0 MPa, (b) 2.5 MPa, (c) 5 MPa, (d) 10 MPa.

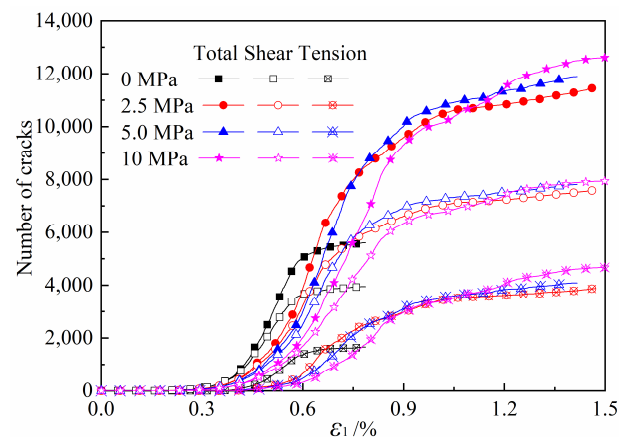


Figure 15. Growth process of crack number in RAC20 under different confining pressures.

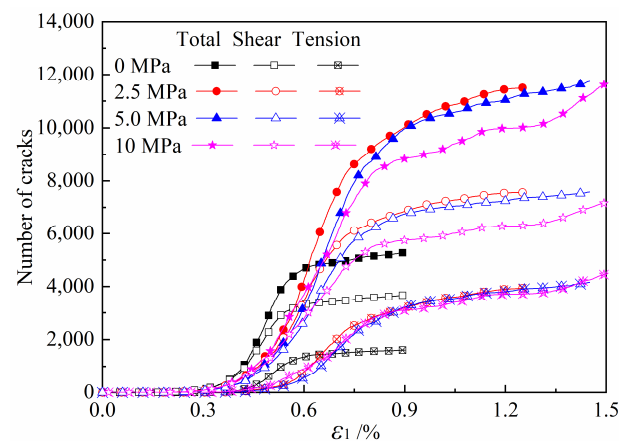


Figure 16. Growth process of crack number in RAC6012 under different confining pressures.

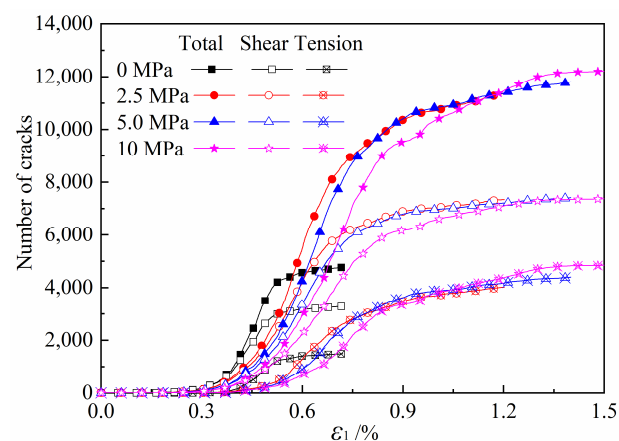
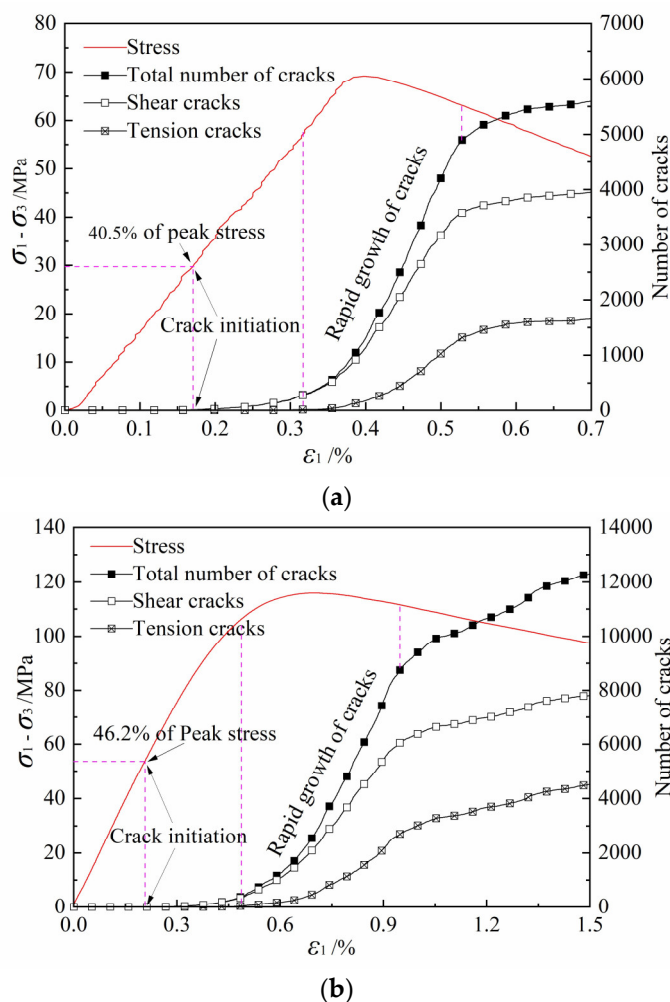


Figure 17. Growth process of crack number in RAC8009 under different confining pressures.

Figure 18 shows the corresponding relationship between the crack development trend and the stress–strain curve. It can be seen from the diagram that when the load reaches 40–50% of the peak stress, cracks begin to appear, and then grow slowly until the loading enters the plastic stage. When the load reaches about 80–90% of the peak stress, the crack growth starts to accelerate, and when the peak stress reaches, the crack growth rate is the largest. After the rapid growth in the peak area, the growth of the number of cracks begins to slow down. At this stage, the expansion of macroscopic through-cracks in the specimen is dominant, and the number of new cracks decreases. Under the action of confining pressure, the occurrence of cracks is delayed. When the confining pressure is

0 MPa, the stress–strain curve of the pre-peak section shows a clear linear relationship, the stress decreases rapidly in the post-peak stage, and the number of cracks increases little. Under the confining pressure of 10 MPa, the pre-peak stress–strain curve presents plastic characteristics, the post-peak stress decreases slowly, and the number of cracks continues to increase.



**Figure 18.** Correspondence between crack development and stress–strain curve under different confining pressures (RAC20). (a) 0 MPa, (b) 10 MPa.

## 5. Conclusions

In this study, the triaxial compression tests of standard curing and steam curing RAC under different confining pressures were carried out first. Then, on the basis of the experimental results, a discrete element model considering the actual coarse aggregate morphology was established, and the triaxial compression process of RAC was simulated and analyzed. The following conclusions are drawn:

The expansion of cracks inside RAC is limited by the confining pressure, and the peak stress and deformation capacity are improved with the increase of confining pressure. Meanwhile, the failure mode of RAC changes from vertical splitting to oblique shearing under the influence of confining pressure. Compared with standard curing, the strength of steam-cured RAC decreases, but it is more sensitive to lateral constraints. Under the same loading conditions, the steam-cured RAC with the lowest strength at 80 °C–9 h is the first to crack, and the total number of cracks and the proportion of tensile cracks in RAC also increases.

The Mohr–Coulomb failure criterion can better reveal the triaxial compression failure mechanism of steam-cured RAC. The results show that high-temperature steam curing significantly reduces the cohesion of concrete, but the internal friction angle is slightly increased. According to the simulation analysis, when the load reaches 40–50% of the peak stress, the crack starts to appear and then grows slowly until the load enters the plastic deformation stage of RAC. When the load reaches about 80–90% of the peak stress, the crack starts to grow at an accelerated rate. When the load reaches the peak stress, the crack growth rate is at a maximum. The increase of confining pressure slows down the growth rate of internal cracks in RAC. However, when the final failure is reached, the internal cracks in RAC develop more fully due to the limitation of the confining pressure, and the number of cracks increases.

**Author Contributions:** Conceptualization, Y.C. and W.X.; methodology, X.C.; software, X.Z.; writing—original draft preparation, Y.C.; writing—review and editing, Y.N.; visualization, Y.C.; supervision, X.C.; funding acquisition, W.X. All authors have read and agreed to the published version of the manuscript.

**Funding:** This research was funded by the Jiangsu Industry University Research Cooperation Project (BY2021059) and the Scientific Research Foundation for High-Level Talents of Jinling Institute of Technology (jit-b-202210).

**Data Availability Statement:** The data that support the findings of this study are available from the corresponding author upon reasonable request.

**Conflicts of Interest:** The authors declare no conflict of interest. The funders had no role in the design of the study; in the collection, analyses, or interpretation of data; in the writing of the manuscript; or in the decision to publish the results.

## References

1. Shehata, N.; Mohamed, O.; Sayed, E.T.; Abdelkareem, M.A.; Olabi, A. Geopolymer concrete as green building materials: Recent applications, sustainable development and circular economy potentials. *Sci. Total. Environ.* **2022**, *836*, 155577. <https://doi.org/10.1016/j.scitotenv.2022.155577>.
2. Khadka, B. Rammed earth, as a sustainable and structurally safe green building: A housing solution in the era of global warming and climate change. *Asian J. Civ. Eng.* **2020**, *21*, 119–136. <https://doi.org/10.1007/s42107-019-00202-5>.
3. Katerusha, D. Investigation of the optimal price for recycled aggregate concrete—An experimental approach. *J. Clean. Prod.* **2022**, *365*, 132857. <https://doi.org/10.1016/j.jclepro.2022.132857>.
4. Ulucan, M.; Alyamac, K.E. A holistic assessment of the use of emerging recycled concrete aggregates after a destructive earthquake: Mechanical, economic and environmental. *Waste Manage* **2022**, *146*, 53–65. <https://doi.org/10.1016/j.wasman.2022.04.045>.
5. de Andrade Salgado, F.; de Andrade Silva, F. Recycled aggregates from construction and demolition waste towards an application on structural concrete: A review. *J. Build. Eng.* **2022**, *52*, 104452. <https://doi.org/10.1016/j.jobe.2022.104452>.
6. Datta, S.D.; Sobuz, H.R.; Akid, A.S.M.; Islam, S. Influence of coarse aggregate size and content on the properties of recycled aggregate concrete using non-destructive testing methods. *J. Build. Eng.* **2022**, *61*, 105249. <https://doi.org/10.1016/j.jobe.2022.105249>.
7. Wang, B.; Yan, L.; Fu, Q.; Kasal, B. A comprehensive review on recycled aggregate and recycled aggregate concrete. *Resour Conserv Recy* **2021**, *171*, 105565. <https://doi.org/10.1016/j.resconrec.2021.105565>.
8. Zheng, Y.; Zhang, Y.; Zhang, P. Methods for improving the durability of recycled aggregate concrete: A review. *J Mater Res Technol* **2021**, *15*, 6367–6386. <https://doi.org/10.1016/j.jmrt.2021.11.085>.
9. Bahraq, A.A.; Jose, J.; Shameem, M.; Maslehuiddin, M. A review on treatment techniques to improve the durability of recycled aggregate concrete: Enhancement mechanisms, performance and cost analysis. *J. Build. Eng.* **2022**, *55*, 104713. <https://doi.org/10.1016/j.jobe.2022.104713>.
10. Ge, P.; Huang, W.; Zhang, J.; Quan, W.; Guo, Y. Mix proportion design method of recycled brick aggregate concrete based on aggregate skeleton theory. *Constr. Build Mater.* **2021**, *304*, 124584. <https://doi.org/10.1016/j.conbuildmat.2021.124584>.
11. Leite, M.B.; Santana, V.M. Evaluation of an experimental mix proportion study and production of concrete using fine recycled aggregate. *J. Build. Eng.* **2019**, *21*, 243–253. <https://doi.org/10.1016/j.jobe.2018.10.016>.
12. Wang, X.; Yang, X.; Ren, J.; Han, N.; Xing, F. A novel treatment method for recycled aggregate and the mechanical properties of recycled aggregate concrete. *J. Mater. Res. Technol.* **2021**, *10*, 1389–1401. <https://doi.org/10.1016/j.jmrt.2020.12.095>.
13. Ouyang, K.; Liu, J.; Liu, S.; Song, B.; Guo, H.; Li, G.; Shi, C. Influence of pre-treatment methods for recycled concrete aggregate on the performance of recycled concrete: A review. *Resour. Conserv. Recy.* **2023**, *188*, 106717. <https://doi.org/10.1016/j.resconrec.2022.106717>.

14. Kou, S.C.; Poon, C.S. Enhancing the durability properties of concrete prepared with coarse recycled aggregate. *Constr Build Mater* **2012**, *35*, 69–76. <https://doi.org/10.1016/j.conbuildmat.2012.02.032>.
15. Alexandridou, C.; Angelopoulos, G.N.; Coutelieris, F.A. Mechanical and durability performance of concrete produced with recycled aggregates from Greek construction and demolition waste plants. *J. Clean Prod.* **2018**, *176*, 745–757. <https://doi.org/10.1016/j.jclepro.2017.12.081>.
16. Zheng, B.T.; Teng, J.G. A plasticity constitutive model for concrete under multiaxial compression. *Eng. Struct.* **2022**, *251*, 113435. <https://doi.org/10.1016/j.engstruct.2021.113435>.
17. Rong, C.; Shi, Q.; Zhang, T.; Zhao, H. New failure criterion models for concrete under multiaxial stress in compression. *Constr. Build. Mater.* **2018**, *161*, 432–441. <https://doi.org/10.1016/j.conbuildmat.2017.11.106>.
18. Azevedo, V.d.S.d.; de Lima, L.R.; Vellasco, P.C.D.S.; Tavares, M.E.d.N.; Chan, T.-M. Experimental investigation on recycled aggregate concrete filled steel tubular stub columns under axial compression. *J. Constr. Steel Res.* **2021**, *187*, 106930. <https://doi.org/10.1016/j.jcsr.2021.106930>.
19. Xu, J.; Wang, Y.; Ren, R.; Wu, Z.; Ozbakkaloglu, T. Performance evaluation of recycled aggregate concrete-filled steel tubes under different loading conditions: Database analysis and modelling. *J. Build. Eng.* **2020**, *30*, 101308. <https://doi.org/10.1016/j.jobe.2020.101308>.
20. Chen, Y.; Chen, Z.; Xu, J.; Lui, E.M.; Wu, B. Performance evaluation of recycled aggregate concrete under multiaxial compression. *Constr. Build. Mater.* **2019**, *229*, 116935. <https://doi.org/10.1016/j.conbuildmat.2019.116935>.
21. Kedir, F.; Hall, D.M. Resource efficiency in industrialized housing construction—A systematic review of current performance and future opportunities. *J. Clean Prod.* **2021**, *286*, 125443. <https://doi.org/10.1016/j.jclepro.2020.125443>.
22. Zairul, M. The recent trends on prefabricated buildings with circular economy (CE) approach. *Clean Technol. Environ. Policy* **2021**, *4*, 100239. <https://doi.org/10.1016/j.clet.2021.100239>.
23. Han, F.; Song, S.; Liu, J.; Huang, S. Properties of steam-cured precast concrete containing iron tailing powder. *Powder Technol.* **2019**, *345*, 292–299. <https://doi.org/10.1016/j.powtec.2019.01.007>.
24. Shi, J.; Liu, B.; Shen, S.; Tan, J.; Dai, J.; Ji, R. Effect of curing regime on long-term mechanical strength and transport properties of steam-cured concrete. *Constr. Build. Mater.* **2020**, *255*, 119407. <https://doi.org/10.1016/j.conbuildmat.2020.119407>.
25. Ramezani-pour, A.M.; Esmaeili, K.; Ghahari, S.A.; Ramezani-pour, A.A. Influence of initial steam curing and different types of mineral additives on mechanical and durability properties of self-compacting concrete. *Constr. Build. Mater.* **2014**, *73*, 187–194. <https://doi.org/10.1016/j.conbuildmat.2014.09.072>.
26. Sebaibi, N.; Boutouil, M. Reducing energy consumption of prefabricated building elements and lowering the environmental impact of concrete. *Eng. Struct.* **2020**, *213*, 110594. <https://doi.org/10.1016/j.engstruct.2020.110594>.
27. Zou, C.; Long, G.; Xie, Y.; He, J.; Ma, C.; Zeng, X. Evolution of multi-scale pore structure of concrete during steam-curing process. *Microporous Mesoporous Mater.* **2019**, *288*, 109566. <https://doi.org/10.1016/j.micromeso.2019.109566>.
28. Zeyad, A.M.; Johari, M.A.M.; Abutaleb, A.; Tayeh, B.A. The effect of steam curing regimes on the chloride resistance and pore size of high-strength green concrete. *Constr. Build. Mater.* **2021**, *280*, 122409. <https://doi.org/10.1016/j.conbuildmat.2021.122409>.
29. Wang, J.; Long, G.; Xiang, Y.; Dong, R.; Tang, Z.; Xiao, Q.; Yang, Z.; Ma, K. Influence of rapid curing methods on concrete microstructure and properties: A review. *Case Stud. Constr. Mat.* **2022**, *17*, e01600. <https://doi.org/10.1016/j.cscm.2022.e01600>.
30. Le Hoang, A.; Fehling, E.; Thai, D.-K.; Van Nguyen, C. Evaluation of axial strength in circular STCC columns using UHPC and UHPFRC. *J Constr Steel Res* **2019**, *153*, 533–549. <https://doi.org/10.1016/j.jcsr.2018.11.001>.
31. Tang, Y.; Fang, S.; Chen, J.; Ma, L.; Li, L.; Wu, X. Axial compression behavior of recycled-aggregate-concrete-filled GFRP–steel composite tube columns. *Eng. Struct.* **2020**, *216*, 110676. <https://doi.org/10.1016/j.engstruct.2020.110676>.
32. Zhu, X.; Chen, X.; Zhang, N.; Wang, X.; Diao, H. Experimental and numerical research on triaxial mechanical behavior of self-compacting concrete subjected to freeze–thaw damage. *Constr. Build. Mater.* **2021**, *288*, 123110. <https://doi.org/10.1016/j.conbuildmat.2021.123110>.
33. Meng, E.; Yu, Y.; Zhang, X.; Su, Y. Experimental and theoretical research on the mechanical performance of totally recycled concrete under triaxial compression after high temperatures. *Constr. Build. Mater.* **2020**, *261*, 120012. <https://doi.org/10.1016/j.conbuildmat.2020.120012>.
34. Cundall, P.A.; Strack, O.D.L. A discrete numerical model for granular assemblies. *Geotechnique* **1979**, *29*, 47–65. <https://doi.org/10.1680/geot.1979.29.1.47>.
35. Mohammadinia, A.; Oskooei, P.R.; Arulrajah, A. Discrete element modeling of cemented recycled concrete aggregates under unconfined and k0 loading conditions. *Transp. Geotech.* **2021**, *26*, 100450. <https://doi.org/10.1016/j.trgeo.2020.100450>.
36. Rangari, S.; Murali, K.; Deb, A. Effect of meso-structure on strength and size effect in concrete under compression. *Eng. Fract. Mech.* **2018**, *195*, 162–185. <https://doi.org/10.1016/j.engfracmech.2018.04.006>.

**Disclaimer/Publisher’s Note:** The statements, opinions and data contained in all publications are solely those of the individual author(s) and contributor(s) and not of MDPI and/or the editor(s). MDPI and/or the editor(s) disclaim responsibility for any injury to people or property resulting from any ideas, methods, instructions or products referred to in the content.